Materials Today Communications 31 (2022) 103649

Contents lists available at ScienceDirect

Materials Today Communications

journal homepage: www.elsevier.com/locate/mtcomm

Irradiation-induced toughening of calcium aluminoborosilicate glasses

Xiangting Ren [a,1], Tao Du [a,1], Haibo Peng [b], Lars R. Jensen [c], Christophe A.N. Biscio [d], Lisbeth Fajstrup [d], Mathieu Bauchy [e], Morten M. Smedskjaer [a,*]

[a] Department of Chemistry and Bioscience, Aalborg University, Aalborg East 9220, Denmark
[b] School of Nuclear Science and Technology, Lanzhou University, Lanzhou 730000, China
[c] Department of Materials and Production, Aalborg University, Aalborg East 9220, Denmark
[d] Department of Mathematical Sciences, Aalborg University, Aalborg East 9220, Denmark
[e] Department of Civil and Environmental Engineering, University of California, Los Angeles, CA 90095, USA

ARTICLE INFO

Keywords:
Oxide glasses
Mechanical properties
Indentation
Irradiation
Molecular dynamics simulations

ABSTRACT

Methods to improve the fracture toughness and strength of glassy materials are increasingly important for a variety of applications that remain limited by the restrictions of brittleness and surface defect propensity. Here, we report on the enhancement of glass mechanical performance through a combination of a tailored chemistry and irradiation post-treatment. Specifically, we show through both experiments and atomistic simulations that the defect (crack) initiation resistance as well as the fracture toughness of selected calcium aluminoborosilicate glasses can be significantly improved (by more than 400% in some cases) through heavy ion irradiation. The ion irradiation process reorganizes the borate subnetwork through a partial transformation of tetrahedral to trigonal boron units, which in turn also modifies the glass at longer lengths scales, such as through a coarsening in the distribution of loop structures. The improvement in both the resistance to crack formation and crack growth is ascribed to the modification of the medium-range glass structure as well as the less rigid network structure upon irradiation with coordination defects that act as local reservoirs of plasticity by allowing more bond switching activities to dissipate mechanical energy upon deformation. This work therefore highlights a new pathway to develop damage-resistant glass materials.

1. Introduction

Low practical strength and brittleness are the main bottlenecks for present and future applications of oxide glasses [1]. Different strengthening methods have been attempted [2], including composition optimization, ion exchange, and pressure treatment. Consistent with the lack of macroscopic brittleness, both molecular dynamics (MD) simulations and experiments suggest the existence of nanoscale ductility in some glasses [3–5]. By nanoscale ductility, we refer to the glasses' ability to deform plastically on the nanometer length scale. For example, flaw-free thin films of amorphous alumina exhibit pronounced plasticity at a high strain rate, which was attributed to bond switching events at the nanoscale, leading to mechanical relaxation and accumulating into macroscopic plastic flow [5]. Additionally, the propensity for bond switching activities of amorphous alumina is encoded in its static structure, which is correlated with the atomic environment of individual Al atoms [6]. Bulk oxide glasses typically exhibit fracture toughness values in the range of 0.5–1 MPa $m^{0.5}$, with all commercially available oxide glasses currently below a value of 1 MPa $m^{0.5}$ [7–9], as measured using self-consistent methods. Fracture toughness values up to 1.17 MPa $m^{0.5}$ have been reported in rare earth containing aluminosilicate glasses [10]. Moreover, in our recent work, we have shown that understanding of nanoscale bond switching activities can be exploited at a larger scale, as we reported a record-high fracture toughness (1.4 MPa $m^{0.5}$) in a bulk oxide glass with high propensity for bond switching[11]. As such, an improved understanding of deformation and fracture mechanisms of glasses at the nanoscale is needed to improve their mechanical performance at the macroscale.

Testing the mechanical properties of glasses by indentation has been a popular method, since it can mimic some types of real-life damage events under controlled conditions [12,13]. That is, sharp contact with a high local stress is the main failure mode in many applications. According to the Vickers indentation response, glasses can be classified as normal, intermediate, or anomalous[14]. Normal glasses deform to a

* Corresponding author.
E-mail address: mos@bio.aau.dk (M.M. Smedskjaer).
[1] These authors contributed equally.

https://doi.org/10.1016/j.mtcomm.2022.103649
Received 27 April 2022; Accepted 2 May 2022
Available online 4 May 2022

large extent due to volume displacing shear[14–17]. For larger indentation crack systems, shear faults play the role of initial cracks, namely, middle/radial and lateral cracks under moderate loads. For anomalous glasses, the deformation is mainly due to volume-reducing densification [18]. The surface tensile stress around the contact will act on the surface defects, thereby forming a ring crack, and the tensile stress at the bottom of the elastic/plastic boundary will promote median cracking. Between normal glasses and anomalous glasses is a third subset named intermediate glasses. Compared with normal glasses, the deformation in these glasses occurs with significantly more densification, and compared with anomalous glasses, their shear deformation is much larger[14]. The intermediate glasses thus eliminate the stresses that lead to ring and median cracks[19]. Some calcium aluminoborosilicate (CABS) glasses have recently been found to belong to the group of intermediate glasses [20]. In these glasses, SiO_2, B_2O_3, and Al_2O_3 are the basic network formers, with the coordination numbers of Si, B, and Al being 4, 3–4, and 4–6 under ambient conditions, respectively[21]. Both 4-fold boron and aluminum need to be stabilized by calcium modifier cations, 5- or 6-fold coordinated aluminum, or oxygen triclusters[22].

The mechanical properties of nuclear waste glass under radiation damage have been studied for decades and the fracture behavior has been found to be altered depending on the irradiation dosage and temperature [23]. This includes studies on heavy ion irradiation treatment of sodium borosilicate (NBS) glasses and the effect on their structure and mechanical properties [24]. Upon irradiation, the indentation hardness of NBS glasses tends to initially decrease and then stabilize with increasing irradiation dose[25]. The difference in irradiation effect on NBS and quartz glasses indicates that the hardness reduction is not only due to the transformation of the silicate network in NBS glasses, but also the transformation of the borate network[26]. MD simulations have also been performed to study irradiated NBS glasses, also showing the decrease in hardness, in agreement with the experimental data [27–30]. Studies have also shown that the elastic modulus of NBS glasses decrease upon irradiation, but the structural changes responsible for these changes in mechanical properties are not well-understood[22].

Considering the high crack resistance of CABS glasses, it is interesting to study the effect of irradiation treatment on their mechanical properties. Recently, we found that the chemical composition of CABS glasses affects their indentation deformation and cracking behavior[22]. Therefore, we here perform irradiation treatment on three different CABS glass compositions (see Table 1). We combine the experimental characterization of hardness, crack resistance, and indentation fracture toughness with MD simulations to explain the changes in these mechanical properties. The investigated glasses have constant CaO content (20 mol%) and varying Si, Al, and B ratios to assess different structural features in the glasses. We perform irradiation treatments with different doses and characterize their structure and mechanical properties using both experiments and MD simulations. The aim is to understand the structural origins for the variation in surface mechanical properties due to irradiation treatment. We note that the experimental data for the as-made glasses (prior to irradiation) are taken from our recent study [22].

Table 1
Nominal chemical compositions of the CABS glasses as well as their measured glass transition temperature (T_g). The glass ID is based on the Al_2O_3 to B_2O_3 ratio. The error in T_g is within ± 2 °C.

Glass ID	SiO_2 (mol%)	Al_2O_3 (mol%)	B_2O_3 (mol%)	CaO (mol%)	T_g (°C)
CABS-0.4	45	10	25	20	665
CABS-0.6	40	15	25	20	668
CABS-0.75	45	15	20	20	683

2. Methods

2.1. Experimental sample preparation

The three CABS glasses (Table 1 and S1) were prepared using the melt-quenching method. $CaCO_3$ (99.5%, ChemSolute), H_3BO_3 (≥99.5%, Honeywell International), Al_2O_3 (99.5%, Sigma-Aldrich), and SiO_2 (≥99.5%, 0.2–0.8 mm, Merck KGaA) were used as the raw materials. First, based on the target composition, the batch of raw materials was thoroughly mixed and gradually added to a Pt-Rh crucible in a furnace at 800 °C to remove H_2O and CO_2. Afterwards, these mixtures were melted at 1600 °C and finally poured onto a steel plate for quenching and transferred to the annealing furnace at the glass transition temperature (T_g)[22]. After annealing, we cut the glasses into the required sizes for the subsequent irradiation and characterization. Based on X-ray diffraction analyses (Empyrean XRD, PANalytical), no signs of crystallization were present in any of the glasses (Fig. S1).

The glass samples (1.7 ×1.2 ×0.1 cm^3) were irradiated with Xe ions at room temperature at the Institute of Modern Physics (IMP), Chinese Academy of Sciences. As shown in Table S2, the penetration depth of the xenon ions (i.e., the thickness of the glass surface layer affected by irradiation) is around 1.7 μm. The xenon ions were generated, selected, and then accelerated toward the sample with an energy of 5 MeV. A pair of grating magnets were used to generate a uniform ion beam that bombards the sample in the target chamber. The pressure in the target chamber was 7×10^{-6} Pa. The typical ion current was 2 μA, and the beam spot size was 20 × 20 mm^2. The samples were treated with two different doses, namely "Dose 1" of 2.0×10^{13} ions/cm^2 and "Dose 2" of 2.0×10^{14} ions/cm^2.

2.2. Experimental sample characterization

The density (ρ) of the glass sample was determined using the Archimedes buoyancy principle (see Table S1). The weight of each sample (at least 1.5 g) was measured ten times in air and ethanol.

Raman spectra were collected using a micro-Raman spectrometer (inVia, Renishaw). The sample surface was excited by a 532 nm green diode pumped solid state laser for an acquisition time of 10 s. The lateral spatial resolution of the Raman measurements is estimated to be around 0.9 μm. The range of the collected spectrum was from 250 to 1750 cm^{-1} and the resolution was better than 2 cm^{-1}. Spectra from five different locations on the glass surface were accumulated for each specimen to ensure homogeneity. All spectra were uniformly treated in Origin software for background correction and area normalization.

Micro-indentation measurements were carried out using a Nanovea CB500 hardness tester to determine the Vickers hardness (H_V), crack resistance (CR), and indentation fracture toughness (K_{IFT}). While hardness quantifies the mean contact stress that is required to form a permanent indentation imprint, both CR and K_{IFT} are related to crack formation upon indentation. Assuming the glass cracks in a controlled and well-defined manner, K_{IFT} is a measure of the glass' resistance to crack growth based on crack length measurements [31], whereas CR is a measure of the glass' resistance to crack initiation based on the statistics of crack-counting at different loads. We therefore rely on both crack length as well as crack counting measurements to characterize the glasses' fracture properties based on indentation.

On each sample, 20 indentations with a maximum load of 4.9 N (0.5 kgf) were generated to determine H_V, with a loading duration of 15 s and dwell time of 10 s. Then we used an optical microscope to analyze the residual imprints and calculate H_V. We also calculated hardness from the force-displacement curves using the Oliver-Pharr model[32,33]. The resistance of the glass to the initiation of corner cracks upon indentation was also determined using the Vickers diamond indenter. We applied increasing loads (from 4.8 to 40 N) and counted the numbers of corner cracks after unloading. CR was calculated according to the method of Wada[34]. To this end, the probability of crack occurrence (PCI) was

determined as the ratio between the number of corners where a corner crack was formed and the total number of corners on all indents. *CR* is then defined as the load that generates two cracks (PCI = 50%) on average per indent. For each sample and each load, at least 30 indents were made with loading duration of 15 s and dwell time of 10 s. Measurements were performed under laboratory conditions (room temperature and relative humidity (RH) of 39 ± 5%).

We also used the indentation method to estimate the resistance against crack growth, i.e., K_{IFT}. This approach is based on a known Young's modulus (see below) and measurements of crack lengths and impression size for a given indentation load[35–37]. We used this method instead of a standard fracture toughness (K_{Ic}) method such as the single-edge precracked beam method, since the irradiation treatment only affects the surface region. However, it is important to note that K_{IFT} from Vickers indentation is often not equal to K_{Ic}, particularly due to the densification that occurs upon indentation[38]. Following the recent work of Gross et al.[14] to avoid or limit this effect, we here determine K_{IFT} using a sharper 100° indenter tip (with same geometry of Vickers but angle of 100° instead of 136°) to minimize the densification component in favor of shear[14]. K_{IFT} is determined using the equation from Anstis et al.[39],

$$K_{IFT} = \xi \left(\frac{E}{H}\right)^{0.5} \left(\frac{P}{C_0^{1.5}}\right) \quad (1)$$

where ξ is an empirically determined constant for a indenter that was calibrated against select materials[39]. E is the Young's modulus, P is the indentation load, C_0 is the average length of the radial/median cracks measured from the center of the indent impression, and H is the hardness. ξ is typically set equal to 0.016 for a Vickers indenter, whereas Gross et al.[14] found that a 110° tip gave a value of 0.0297. We used these values to extrapolate to a value of $\xi = 0.035$ for the 100° tip used in the present study. We chose an indentation load of 3 N, since it is just high enough to produce corner cracks from the indent impressions. On each sample, six indentations were generated, with a loading duration of 15 s and dwell time of 10 s. The crack lengths and major diagonal lengths were then measured and combined with values of E and H to calculate K_{IFT}. By assuming $K_{IFT} = K_{Ic}$, we also calculated the fracture energy (G_c) to enable comparison with the MD simulations results following Irwin's formula (in plane strain)[40],

$$G_C = \frac{1-\nu^2}{E} {K_{IFT}}^2 \quad (2)$$

where ν is the Poisson's ratio.

The elastic properties of the glasses were measured by ultrasonic echography using an ultrasonic thickness gauge (38DL Plus, Olympus) equipped with 20 MHz delay line transducers for the determination of the longitudinal V_1 and transversal wave velocities V_2. The experimental data for the as-made glasses (prior to irradiation) are taken from our recent study[22].

To probe the irradiation-induced change in surface elasticity, the Oliver-Pharr method was used to calculate the reduced elastic modulus (E_r) of the CABS glass surfaces. These measurements were carried out using a Nanovea CB500 hardness tester with a Vickers indenter tip. The load-depth curve was obtained through the indentation test, and E_r was then calculated as,

$$S = \frac{2}{B\sqrt{\pi}} E_r \sqrt{A_{Pml}} \quad (3)$$

$$\frac{1}{E_r} = \frac{1-\nu^2}{E} - \frac{1-\nu_i^2}{E_i} \quad (4)$$

where S is the contact stiffness, B is a geometrical factor depending on the indenter[32], A_{pml} is the projected area, and E and ν are the elastic modulus and Poisson's ratio of the sample (from ultrasonic echography tests), and E_i and ν_i are the elastic modulus and Poisson's ratio of the indenter. Based on these, we could calculate the reduced elastic modulus (E_r).

2.3. Simulation details

The classical MD simulations in this study were carried out using the GPU-accelerated LAMMPS software[41], and visualization of the configurations were performed with the OVITO package[42]. Periodic boundary conditions were applied in all directions during the simulations. The interaction between the constituent atoms (Ca, Al, B, O, and Si) were described with a Buckingham-Coulomb potential, following the parametrization by Du et al.[43,44]. The cutoff for Buckingham and Coulombic interactions was 10 Å. Long-range Coulombic interactions were computed using the Particle-Particle Particle-Mesh (PPPM) algorithm with an accuracy of 10^{-5}. This potential has previously been used and validated in various multicomponent oxide glasses, including aluminosilicate[45], phosphate[46], borate[47], and borosilicate[48] glasses. For comparison, we also adopted another potential from Ref. [49] to simulate the pristine glasses. The structural and mechanical properties shown in Fig. S2 and Table S3 indicate that the potential by Du et al. [43] is more suitable for the glass compositions in this study. Considering the ballistic cascades during the irradiation simulations (see Section 2.5), the short-range repulsive interactions were modified by the Ziegler-Biersack-Littmark (ZBL) potential[50] coupled with high-order polynomials to ensure the smoothness of the energy, force, and their derivatives as a function of interatomic distance. The motion of atoms was described using the velocity-Verlet integration algorithm with a fixed timestep of 1 fs, except in the simulation of ballistic cascade, where we used a variable timestep to avoid the unrealistic configuration generated by the high velocity collisions.

2.3.1. Simulation of melt-quenched glasses

The glass formation was simulated by the conventional melt-quenching method. The initial configurations were generated by randomly placing the atoms into a cubic box based on the experimental density, while ensuring the absence of any unrealistic proximity of atoms by using the PACKMOL package[51]. The compositions of glasses were the same as the experimental samples, and the constituents of each simulated system are given in Table 2.

The resulting configurations were then subjected to potential energy minimization to adjust the structural geometry. Afterwards, these structures were melted at 5000 K in the *NVT* ensemble with a Nosé –Hoover thermostat[52] for 100 ps to ensure that the memory of the initial configuration had been completely erased. After the melting process, the systems were linearly cooled down to 300 K during 1 ns in the *NVT* ensemble. Finally, the glasses were successively equilibrated at 300 K in the *NPT* ensemble at zero pressure and then in the *NVT* ensemble for 60 ps to remove the internal stress and obtain the density information. The simulation box was further equilibrated in the *NVT* ensemble for 100 ps to generate 100 frames of trajectory to compute structural and thermodynamic properties.

2.3.2. Simulation of irradiation process

To match the size of samples for the following fracture simulations, the melt-quenched glass structures were duplicated by 2 × 2 × 1 along the three directions, thus now consisting of more than 14,000 atoms (dimensions of 70 ×70 ×35 Å^3). These glasses were subjected to

Table 2
Chemical constitutions (number of atoms) of the glass models simulated herein.

Glass ID	CaO	Al_2O_3	B_2O_3	SiO_2	Total atoms
CABS-0.4	200	100	250	450	3500
CABS-0.6	200	150	250	400	3600
CABS-0.75	200	150	200	450	3500

simulated irradiation using a well-established methodology by initiating a series of displacement cascades[53–56]. In each cascade, we randomly selected an atom and accelerated it with a kinetic energy of 500 eV along a random direction. The selected atom, also known as the primary knock-on atom (PKA), was alternating as projectiles and collided with the nearby atoms in the glass, thereby resulting in a ballistic cascade. Subsequently, a spherical region was created around the PKA with a radius of 10 Å, which was defined as the impacted zone. The dynamics of the atoms inside the impact zone were then equilibrated in the *NVE* ensemble, outside of which atoms were kept at a constant temperature of 300 K using a Berendsen thermostat. Note that, during this ballistic cascade, a variable timestep was used to avoid the unrealistic configuration generated by the high velocity collisions. The simulation of the cascade had a length of 20 ps, which was found to be long enough for the system to relax and converge its thermodynamic quantities (i.e., energy, temperature, and pressure), thereby confirming the PKA had come to rest in the glass. After each collision, the system was further relaxed in the *NPT* ensemble at 300 K and zero pressure for 5 ps to adjust its configuration and volume upon irradiation. The above process was iteratively repeated with different PKAs until the system reached saturation in terms of enthalpy and density.

2.3.3. Structure analysis of simulated glasses

The melt-quenched glass structures before and after irradiation were analyzed in terms of the bond angle distribution (BAD), ring size distribution, neutron structure factor ($S(Q)$), and persistence diagrams. The ring distribution was calculated using the RINGS package[57], wherein a ring structure is defined as the shortest closed path within the network formers connected by O atoms[58] and the ring size is defined in terms of the number of Al, B, and Si atoms in a ring. $S(Q)$ was computed using the Faber–Ziman formula[59] through the Fourier transformation of the pair distribution function ($g(r)$) as described in Ref.[60].

To better characterize the irradiation-induced medium-range order structural changes, we used persistent homology. Persistent homology is a tool within topological data analysis that has been used to analyze the qualitative features of high-dimensional data such as point cloud data set across multiple scales. By regarding the atomic configuration as a point cloud data set, the hierarchical structural features of materials can be extracted at different scales. Based on these features, persistent homology has shown great promise in analyzing the medium-range structure of different glass systems such as oxide[61–63] and metallic glasses [62,64], as well as glass structure under pressure[63] or chemical replacement[65].

In this study, persistent homology analysis to determine persistence diagrams was carried out using the Diode[66] and Dionysus 2[67] packages. As mentioned in Refs. [68,69], the procedure for obtaining the persistence diagram is as follows: 1) Each atom is replaced by a ball with its atomic radius, and then the radius of each ball is gradually increased with the same increment. 2) Consisting at first of points (the center of the atoms), line segments p_ip_j connecting pairs p_i, p_j of points are added when the growing ball with center p_i and the one with center p_j intersect. Triangles $p_ip_jp_k$ are added when the balls with center p_i, p_j and p_k all have a common intersection, whereas a tetrahedron $p_i\ p_j\ p_k\ p_l$ is added when the four balls have a common intersection. If, during this process, all the edges in a closed sequence $p_{i1}\ p_{i2}$, $p_{i2}p_{i3}$, …, $p_{ik}p_{il}$ have been added, a loop is *born* at the time when the last edge is added. The loop *dies* when enough triangles have been added to fill it in or connect it to another loop, indicating that it does not surround a unique "hole" in the structure anymore. Note that an edge p_ip_j does not necessarily represent a chemical bond, as it is purely geometry. The persistence diagram is the scatter plot of the points (b_i, d_i), where b_i denotes the birth time and d_i denotes death time of each loop. The atomic radii of each element was defined by following the approach in Ref. [68], specifically $r_{Al} = 0.483$ Å, $r_B = 0.158$ Å, $r_{Ca} = 1.083$, $r_O = 1.280$ Å, and $r_{Si} = 0.333$ Å.

2.3.4. Fracture simulations

The as-made and irradiated glasses were subjected to fracture simulations for qualitative comparison with the experiments. We simulated the mode I fracture, i.e., with loading in perpendicular direction to the crack plane. The fracture energy was calculated using the method of Brochard et al.[70], which is based on the energetic theory of fracture mechanics and does not involve any assumptions of the material behavior. Therefore, this method can be used in calculating the fracture energy of both brittle and ductile systems[71–73]. In order to minimize the size effect, the samples were further duplicated by $2 \times 2 \times 1$ (thus $4 \times 4 \times 1$ supercells of the melt-quenched glasses), yielding a system size of about $140 \times 140 \times 35$ Å^3 (~56,000 atoms). A precrack was introduced by removing the atoms in an ellipsoidal cylinder with a length of 1/3 and a height of 1/15 of the box dimension in the loading direction. The crack size was selected based on the crack size dependence of the fracture energy as shown in Fig. S3. Before applying stress, the system was equilibrated in the *NPT* ensemble at 300 K and zero pressure for 100 ps relaxation, which was found to be long enough for the potential energy of the new system to converge. Afterwards, the sample was subjected to uniaxial tensile loading by deforming the structure along the x-direction at a constant strain rate of 5×10^8 s^{-1}, while the dimensions in the y- and z-directions were free to deform so as to exhibit zero stress along these directions. During the fracture simulations, the system was maintained in the *NPT* ensemble, and the temperature and pressure were controlled by the Nosé –Hoover thermostat and barostat, respectively[52,74]. Strain and the corresponding stress in the loading direction were recorded until a total strain of 50%. Young's modulus was determined as the slope of the stress-strain curve in the low strain region ($\varepsilon < 0.05$) using linear regression. The fracture energy was calculated by integrating the stress-strain curve up to the failure strain,

$$G_C = \frac{L_yL_z}{\Delta A}L_x \int_0^{\varepsilon_{xx}^f} \sigma_{xx} d\varepsilon_{xx} \tag{5}$$

where G_C is the fracture energy, L_x, L_y, and L_z are the dimensions of the simulation box, ΔA is the newly created surface area upon fracture, ε_{xx}^f is the strain in the x-direction when the stress dropped to zero, and σ_{xx} and ε_{xx} are the recorded stress and strain, respectively, in the x-direction. The surface areas were calculated based on a surface mesh construction algorithm implemented in the OVITO package[42,75]. Specifically, the surface mesh was constructed through a spherical probe with a radius of 3.6 Å combined with a smoothing level of 10 to ensure a sufficient accuracy and no artificial voids.

2.3.5. Bond switching analysis

The bond breaking and re-formation events during the fracture process was characterized by the bond switching activities as a function of the applied tensile strain. The bond switching analysis was done on the Al, B, and Si atoms. That is, the fraction of atoms with a decreased, increased, or unchanged coordination number (CN) was calculated by comparing the CN of each individual atom with its initial CN at non-strained state. The swapped CN is defined as an unchanged CN for which at least one oxygen neighbor is exchanged with another one.

3. Results and Discussion

3.1. Structure of experimental glasses

Fig. 1a shows the micro-Raman spectrum of the as-made and irradiated CABS-0.6 glass (Dose 1), while the corresponding spectra for the two other glass compositions are shown in Fig. S4. We divide the spectra into four main bands from *I* to *IV* and outline the expected assignments in the following. Band region *I* (~250–625 cm^{-1}) is expected to contain contributions originating from B-O-B, Al-O-Al, and B-O-Al stretching bands. Besides, vibrations due to superstructural units such as pentaborates may occur in this region. Furthermore, Si-O-Si network units

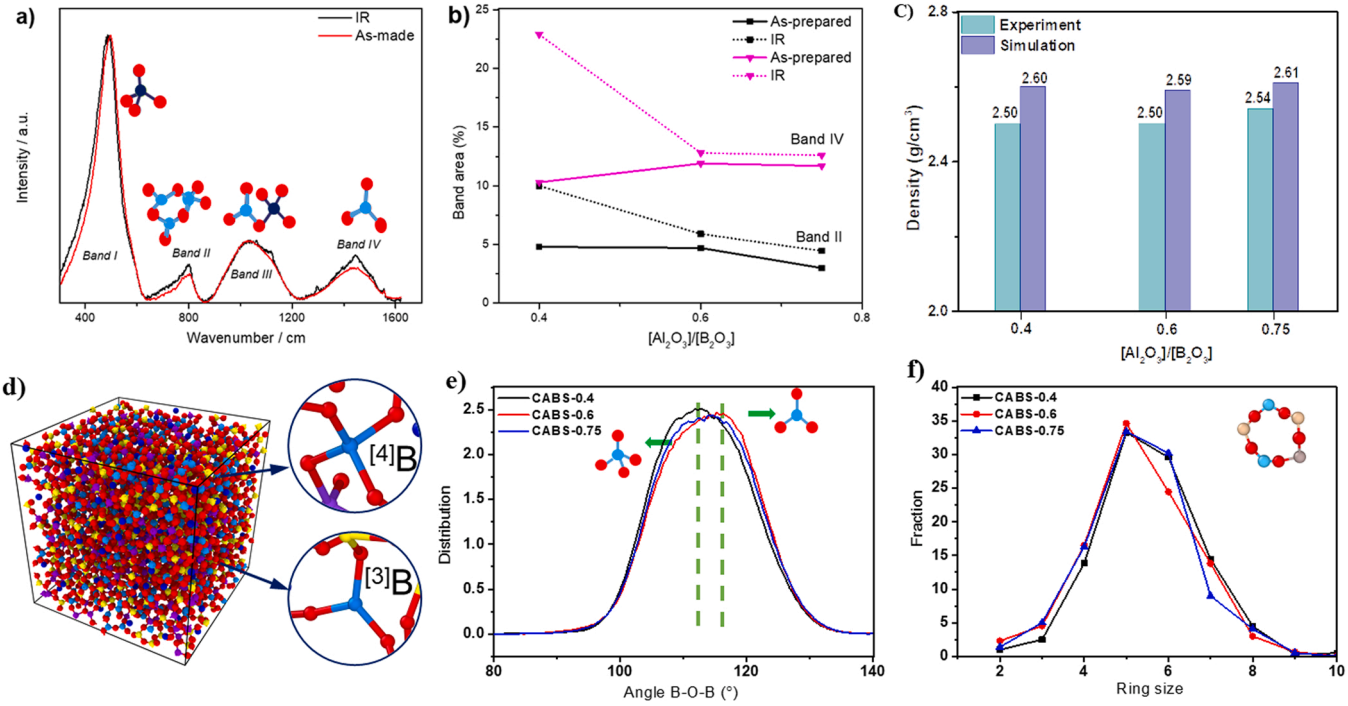

Fig. 1. (a) Micro-Raman spectra of the as-made and irradiated (IR) CABS-0.6 glass. The assignment of the four band regions are discussed in the text. (b) Relative area fractions of the two main Raman bands (bands *II* and *IV*) for as-made and irradiated CABS glasses. (c) Comparison of the experimental and simulated density of the as-made glasses. (d) Atomic snapshot of the simulated as-made CABS-0.6 glass, consisting of 3600 atoms. Al, B, Ca, O, Si atoms are represented by purple, cyan, blue, red, and yellow spheres, respectively. (e) Simulated O-B-O bond angle distribution and (f) ring size distribution in the CABS glasses.

may also occur in this region[76]. Band region *II* (~625–860 cm^{-1}) is characteristic for B_2O_3-rich glasses[76], since peaks in this frequency range are typically assigned to borate superstructures such as chain and ring metaborates[77,78], di-triborates[79], and penta-, tetra-, or triborates[77,80], as well as boroxol rings[77,81]. In addition, B-O-Al stretching and aluminate network may occur in this region. The presence of triborates (~770 cm^{-1}) and ditriborates (~755 cm^{-1}) may also be found in this region, considering the high intensity in this range of wavenumbers and the fact that they consist of both $^{[3]}$B and $^{[4]}$B units. The Si-O stretching vibration also contributes (800 cm^{-1}). Band region *III* (~860–1200 cm^{-1}) is expected to contain contributions originating from the Q^n species (SiO_4 units with *n* bridging oxygens)[76], with bands at 1000 cm^{-1} attributed to the stretching Si-O vibration in Q^2 species[82]. Finally, band region *IV* (~1200–1600 cm^{-1}) is typically assigned to signal contributions from vibrations of $^{[3]}$B units[83].

Fig. 1a-b also show that compared to the as-made CABS glasses, the areas of bands *II* and *IV* increase upon irradiation with two different doses (Fig. S4). This suggests that the irradiation treatment (at two different doses) mainly influences the structure around the B units in the CABS glass structure, which is also consistent with previous studies[25,84]. Moreover, we have collected micro-Raman spectra on indented glasses (Fig. S5), for which the stress increases toward the center of the indent[85]. For the irradiated glasses, the structural changes induced by indentation are more obvious compared to those for the as-made glasses. Specifically, the indentation most influences bands *II* and *IV*, similarly to the results in Fig. 1a for irradiation-induced changes.

3.2. Structure of simulated glasses

To examine the ability of the utilized MD potential to reproduce the properties of the CABS glasses, we first analyze the structure of the different glass compositions. Fig. 1c shows the composition dependence of density of the as-made glasses. Although the simulated densities are slightly overestimated (by about 3.8%), the compositional scaling of density is well-reproduced, i.e., the CABS-0.75 and CABS-0.6 glasses exhibit the largest and lowest density, respectively. An atomic snapshot of the as-made CABS-0.6 glass is shown in Fig. 1d, illustrating the coexistence of $^{[3]}$B and $^{[4]}$B units in the glass structure.

We then analyze the short- and medium-range structures of the as-made glasses by calculating the pair distribution, bond angle distribution, and ring size distribution. As shown in Fig. S6, all the compositions exhibit three peaks in the pair distribution function, which are assigned to the B-O (1.45 Å), Si-O (1.60 Å), and Al-O (1.76 Å) bonds, respectively. The distribution of O-B-O bond angle is shown in Fig. 1e, providing evidence for the existence of both $^{[3]}$B and $^{[4]}$B units. Specifically, the tetrahedral $^{[4]}$B unit with O-B-O angle of about 109° and the planar $^{[3]}$B unit with O-B-O angle of 120°. We find that the fraction of $^{[4]}$B units decreases in the order CABS-0.4 > CABS-0.75 > CABS-0.6. The ring structures containing Al, B, Si, and O atoms are used to characterize the medium-range structure in the as-made glasses. As shown in Fig. 1f, most of the rings in all three glasses are five-membered rings, in good agreement with simulation results for related borosilicate glasses [86].

Fig. 2a shows how the average CN of B decreases monotonically and eventually reaches a constant value in all the glasses with an increase in the deposited energy. That is, the irradiation induces the partial conversion of $^{[4]}$B to $^{[3]}$B. These findings echo the experimental Raman results, showing irradiation-induced $^{[4]}$B to $^{[3]}$B conversion (Fig. 1a). Interestingly, despite the differences in the initial CN of B in the three glasses, the final CN of B reaches a value of around 3.3 when the irradiation energy saturates. On the other hand, there is no observe obvious changes of CN of Al and Si atoms upon irradiation (see Figs. S7a and S7b). In addition, Fig. 2b shows that the densities of the CABS glasses also decrease and then reach a plateau value upon irradiation, consistent with the literature[86–88]. As shown in Fig. 2c, the enthalpy becomes less negative and eventually saturates upon irradiation. Since the enthalpy is mostly influenced by the short-range structure[53], the increase of enthalpy is mainly attribute to the formation of $^{[3]}$B species, which is favored at higher temperatures caused by irradiation events [86]. We have confirmed this by calculating the distribution of enthalpy

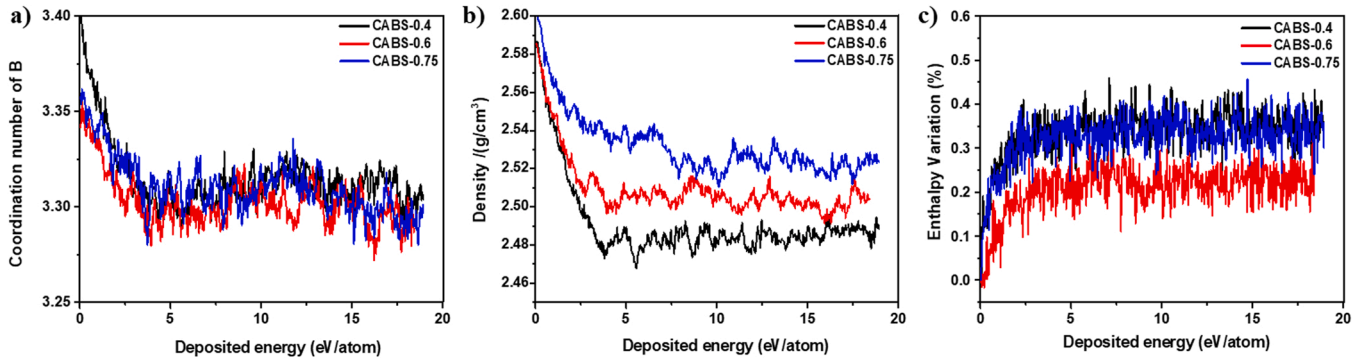

Fig. 2. Evolution of (a) average coordination number of B, (b) density, and (c) normalized enthalpy changes of CABS glasses as a function of the deposited energy during the simulated irradiation process.

per atom of $^{[3]}$B and $^{[4]}$B as shown in Fig. S8. This phenomenon is similar to an increase in fictive temperature of the glass—it becomes less stable, and more similar to a hyperquenched glass. Additionally, through the cluster analysis of $^{[3]}$B atoms, the irradiated glass remains in a homogeneous state despite the increased number of $^{[3]}$B after irradiation (see Fig. S9).

As shown in Fig. 3a for the CABS-0.4 glass, the O-B-O bond angle distribution shifts towards a higher angle upon irradiation, which manifests itself through the increase of intensity of the 120° angle at the expense of the 109° angle (results of the other compositions are shown in Fig. S10). Among the three compositions, the CABS-0.4 glass exhibits the most pronounced structural changes upon irradiation, potentially because it has the highest fraction of $^{[4]}$B units in the as-made glass (see Fig. 1e). Next, we focus on the effect of irradiation on the ring structures. As shown in Fig. 3b for the CABS-0.4 glass, the ring size distribution exhibits some coarsening upon irradiation, wherein the fractions of some small rings (i.e., three- and four-membered) and large rings (i.e., seven-membered and larger) increase at the expense of intermediate-sized rings (i.e., five-membered), in agreement with the behavior for other irradiated silicate glasses[53,86]. The results for the other compositions can be found in Figs. S10c and S10d. As shown in Fig. 3c, we generally find that the simulated neutron structure factors for different irradiated states are similar, with minor differences observed for the first sharp diffraction peak (FSDP) (see results of the other compositions in Fig. S11). Specifically, the FSDP slightly shifts towards to a lower Q value while its intensity decreases with an increase in the deposited energy, indicating an increased disorder in the medium-range structure and swelling of CABS glasses upon irradiation.

To characterize the irradiation-induced structural changes at different length scales, we rely on persistent homology analysis of the simulated glass structures. As shown in Fig. 3d-f, we observe that the distribution of the characteristic regions in the persistence diagrams starts to diffuse to the high-death regions upon irradiation, especially in the low-birth region (i.e., loops are chemically bonded like ring structures), indicating that the sizes of the loops increase upon irradiation. This result is in agreement with the results of Figs. 3b and 3c,

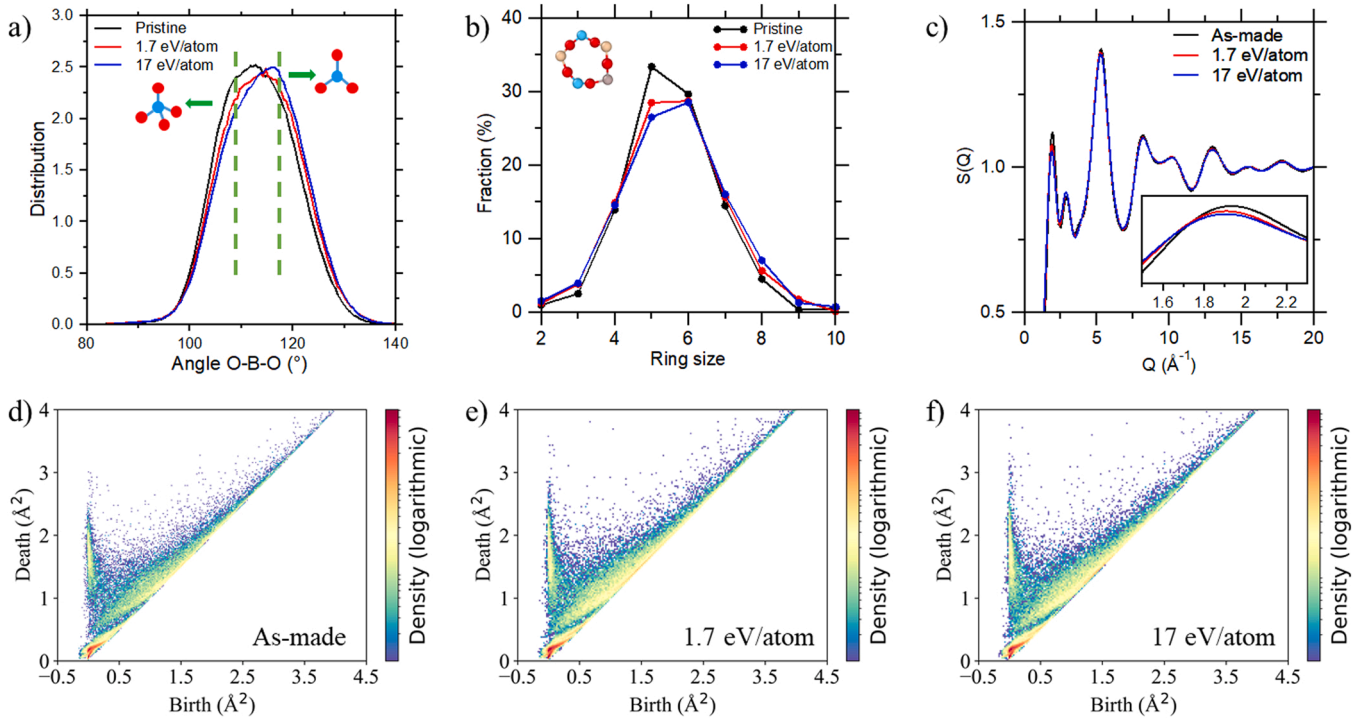

Fig. 3. (a) Simulated O-B-O bond angle distribution, (b) ring size distribution and (c) simulated neutron structure factor of the CABS-0.4 glasses subjected to different amounts of irradiation energies, namely, 0, 1.7, and 17 eV/atom. (d-f) Persistence diagrams for CABS-0.4 glass structure for (d) as-made state and subjected to irradiation with dose of (e) 1.7 eV/atom, and (f) 17 eV/atom.

demonstrating that irradiation changes the medium-range order structure of CABS glasses (results of the other compositions are in Fig. S12).

We further calculated the quantities of persistence diagrams at different regions to compare the structural changes upon irradiation. As shown in Fig. 4a, the high-density region in the red dashed box with low birth and death values correspond to the short-range order structure, e.g., chemically bonded three-membered loops. The structural features of network formers (i.e., Al, B and Si atoms) are analyzed through the persistence diagram of configuration with only Si, B, and Al elements. As shown in Fig. 4b, there is a dispersed curve at a low-birth region, which corresponds to the loop structure consisting of network formers. Since the birth values are around 2 Å^2, the edge of the loop structure is estimated to be around 3 Å, close to the distance of two Si atoms bonded by a bridging oxygen atom.

We then calculate the total loop numbers per atom for pristine and irradiated glasses (Fig. 4c), showing that the loop numbers in all three glasses are reduced upon irradiation, i.e., a less connected structure appears after irradiation. When grouping the 3-membered loops based on their types, we find that most of the 3-membered loops are in the form of O-Al-O, O-B-O, and O-Si-O. Fig. 4d-f show the changes in the different loop numbers, revealing that most of the 3-membered loops are O-Si-O type. After irradiation, the number of O-Si-O and O-B-O loops decrease. For O-B-O, the number decreases as the CN decreases. However, since the CN of Si remains constant upon irradiation, the reduction of loop numbers indicates the distortion of SiO_4 tetrahedra. The histograms of death values in the red dashed box region of Fig. 4b are shown in Fig. 4g-i. We observe that all the distributions become more dispersed upon irradiation. Given that the death values are correlated with the loop sizes, these results suggest a broader distribution of various loop structures, which agrees well with the results shown in Fig. 1f and Figs. S10(c, d).

We further calculated the accumulated persistence function (APF) for loops in the glass structures based on these persistence diagrams (see Fig. S13). APF is a cumulative sum of all points in the persistence diagram weighted by their "lifetime" (d_i - b_i), which quantifies how close neighboring atoms are in a loop and weighs it against the separation of the most distant atoms. Here, we observe that the shapes of the APF curves are qualitatively similar for all the glasses before and after irradiation. However, the maximum value decreases with increasing value of the deposited energy. Since the value of APF represents the number of loops[69], these results further confirm the irradiation-induced swelling and decreased connectivity in the CABS glass structure. Overall, we conclude that irradiation not only influences the short-range structure (e.g., $^{[4]}$B to $^{[3]}$B conversion), but also the medium-range order (e.g.,

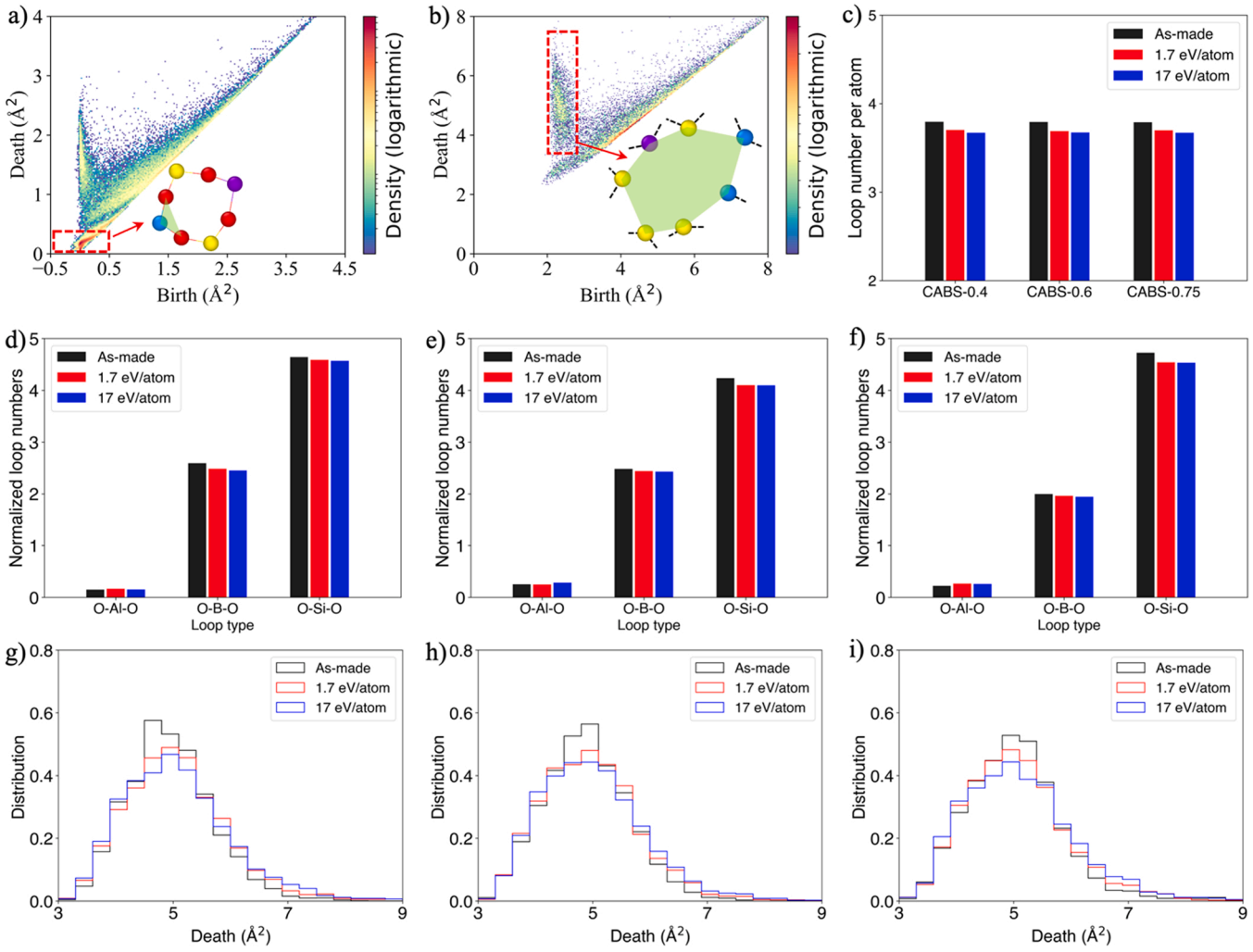

Fig. 4. Schematic of (a) short-range structure (i.e., 3-membered loop) in the persistence diagram of CABS-0.4 glass before irradiation and (b) medium-range structure in the persistence diagram of configuration with only Si, B, and Al elements in CABS-0.4 glass before irradiation. (c) Loop number per atom in simulated CABS glasses of different irradiated states. Note that the loop numbers are normalized by the number of each cation type. (d-f) Numbers of different 3-membered loops in the as-made and irradiated states of (d) CABS-0.4, (e) CABS-0.6, and (f) CABS-0.75 glasses. (g-i) Distributions of death scales in the red dashed box region of (b) in the pristine and irradiated states of (g) CABS-0.4, (h) CABS-0.6, and (i) CABS-0.75 glasses.

loop sizes increasing with reduced loop numbers).

3.3. Experimental mechanical properties

The experimental determination of micro-mechanical properties using the micro-indentation is schematically illustrated in Fig. 5a. Based on the experimental indentation test, the related micro-mechanical properties of CABS glasses before and after irradiation were explored, including the hardness (H_v), crack resistance (CR), and indentation fracture toughness (K_{IFT}). Here, CR reflects the resistance for crack initiation while K_{IFT} represents the resistance of crack propagation.

Fig. 6a shows Young's modulus data for the as-made and irradiated CABS glasses. For the as-made glasses, the modulus was measured by ultrasonic echography, but the values were also determined from the load-depth curves (see Fig. S14) based on the indentation test, since the irradiation process only affects the surface region (~1.7 μm, see Table S2). The absolute values differ between the two tests, as also reported previously for other glasses[89], but the compositional trend is the same. The modulus values of the irradiated CABS glasses derived from indentation decrease compared to the as-made glasses, with a larger decrease for a larger irradiation dose. The decrease of modulus may be explained by the density and structural changes. That is, the less rigid and open structure of $^{[3]}$B can likely explain the decrease in modulus upon irradiation[90], since modulus is mainly controlled by the bond strengths and the number of bonds per volume[91]. In addition, Kieu et al. found that the decrease in modulus is proportional to the increase in the fraction of $^{[3]}$B atoms in the glass network[92]. The transition from $^{[4]}$B to $^{[3]}$B also allows the formation of more non-bridging oxygens. That is, the Ca^{2+} ions that originally charge-compensated the [BO_4] groups can be converted into a network modifier that is connected to the SiO_4 unit. In addition, based on the medium range structural changes (see Fig. 3c-f), the formation of larger loops will decrease the bond density, also contributing to the reduced modulus after irradiation.

Fig. 6b shows the hardness data for the as-made and irradiated CABS glasses. Hardness decreases upon irradiation, consistent with previous findings for hardness of some borosilicate glasses irradiated with different ions[84,91,93,94]. The changes in hardness of the samples under different doses is more pronounced when performing the indentation using a smaller load (0.1 N), with the irradiation-induced decrease of hardness being positively correlated with the dose (Fig. S15). Structural analysis from both Raman and MD simulations indicates that some of the four-coordinated B atoms transform into the three-coordinated B atoms after irradiation. $^{[3]}$B has a more open structure as it does not require charge compensation, and $^{[3]}$B also has a planar structure, which makes it easier to undergo densification and increase its coordination number during indentation[90]. Studies indicate that the larger the fraction of three-coordinated B, the larger the decrease in hardness[95]. Therefore, due to the free volume accumulation and reduction of boron coordination in parallel with the formation of non-bridging oxygen, plastic deformation will be promoted, which will also result in the decrease in hardness[96]. Fig. 6c shows the load dependence of hardness for the CABS-0.4 glass, with an initial decrease in hardness with the increase of applied load for the as-made sample before it reaches an approximately constant value. For the irradiated sample, as the applied load increases, the hardness of the sample first decreases first, then slightly increases, and finally it also reaches a constant value. The smallest hardness is at about 1.7 μm for the irradiated glass (Fig. S16), then slowly increases and then stabilizes, which may also be related to the reduced hardness of the irradiated layer. In the process of indentation, as the applied load increases, the corresponding depth also increases, and the proportion of the irradiation layer will be relatively reduced.

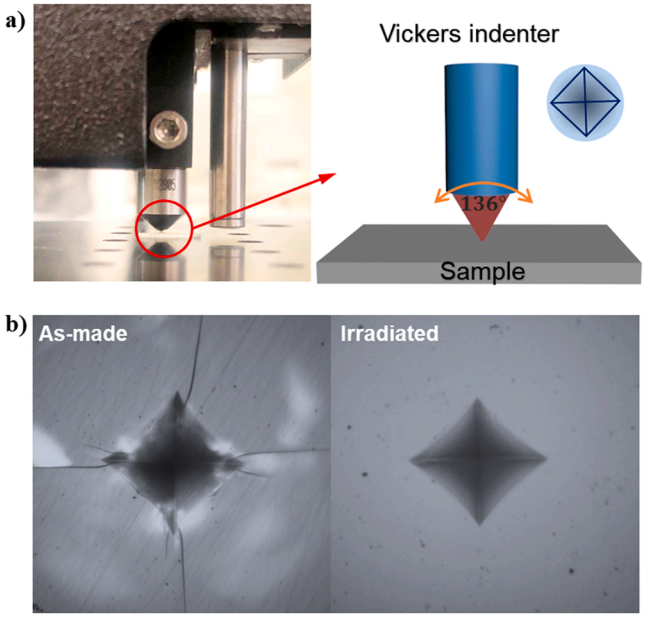

Fig. 5. (a) Example of Vickers indentation of the CABS-0.4 glass. (b) Optical images of indents produced at 15 N on the surface of the as-made (left) and the irradiated (right) CABS-0.4 glasses, respectively.

Based on optical images of indents (Fig. 5b), we find that the crack resistance of the irradiated glasses increases compared to the as-made glasses. That is, the optical images for indentation under 15 N for the three irradiated CABS glasses show no cracks compared to the as-made glasses, which exhibits a higher damage-resistant behavior after irradiation. Fig. 6d shows the crack resistance for the as-made and irradiated CABS glasses, with the individual crack probability vs. load curves shown in Fig. S17. *CR* increases upon irradiation, specifically, crack resistance increased by more than 400% (from 5.6 N to 28 N) for the irradiated CABS-0.75 glass compared to the as-made one. Based on the MD simulation results (Fig. 2a), it can be found that the initial CN of B in CABS-0.4 and CABS-0.75 is relatively higher than that in CABS-0.6 before irradiation, and eventually reaches a constant value in all the glasses with an increase in the deposited energy. This indicates that for CABS-0.4 and CABS-0.75 glasses, the transition from $^{[4]}$B to $^{[3]}$B is more pronounced, which is consistent with the trend of CR change in the experiment.

It has been shown that the residual stress is the driving force for the radial crack[97–99]. Based on the expanding cavity model, densification serves as an alternative to the plastic zone expansion under the indenter [99]. Therefore, the densification deformation tends to produce less residual stress and less subsurface damage, as a result, the threshold load required to initiate cracks increases. In other words, crack resistance usually increases with the increasing contribution of densification under the indenter. Studies have shown that the high shear deformation tendency of boron atoms and the easiness of boron coordination transformation under load improve the crack resistance [100]. For these mechanisms to be effective, it is not just the boron content that is important, but the initial threefold boron content in the glass. Therefore, as the four-coordinated B is transformed into the three-coordinated B after irradiation, the "reversible" coordination change of CABS under indentation helps to improve its crack resistance as it dissipates energy and reduces stress accumulation[100].

Fracture toughness is an important property used in glass fracture mechanics to predict the combination of stress and defect size required for fracture. In this study, an indentation test was performed on CABS glass to calculate the indentation fracture toughness (K_{IFT}) (Table S4). As shown in Fig. 6e, irradiation treatment causes K_{IFT} to increase, with a larger increase for a larger irradiation dose. We have also calculated the fracture energy (G_c) from the K_{IFT} data (Table S5). Fig. 6 f shows that the G_c of CABS glass increases after irradiation. Interestingly, we also observe that the most toughening occurs for the CABS-0.4 glass, which

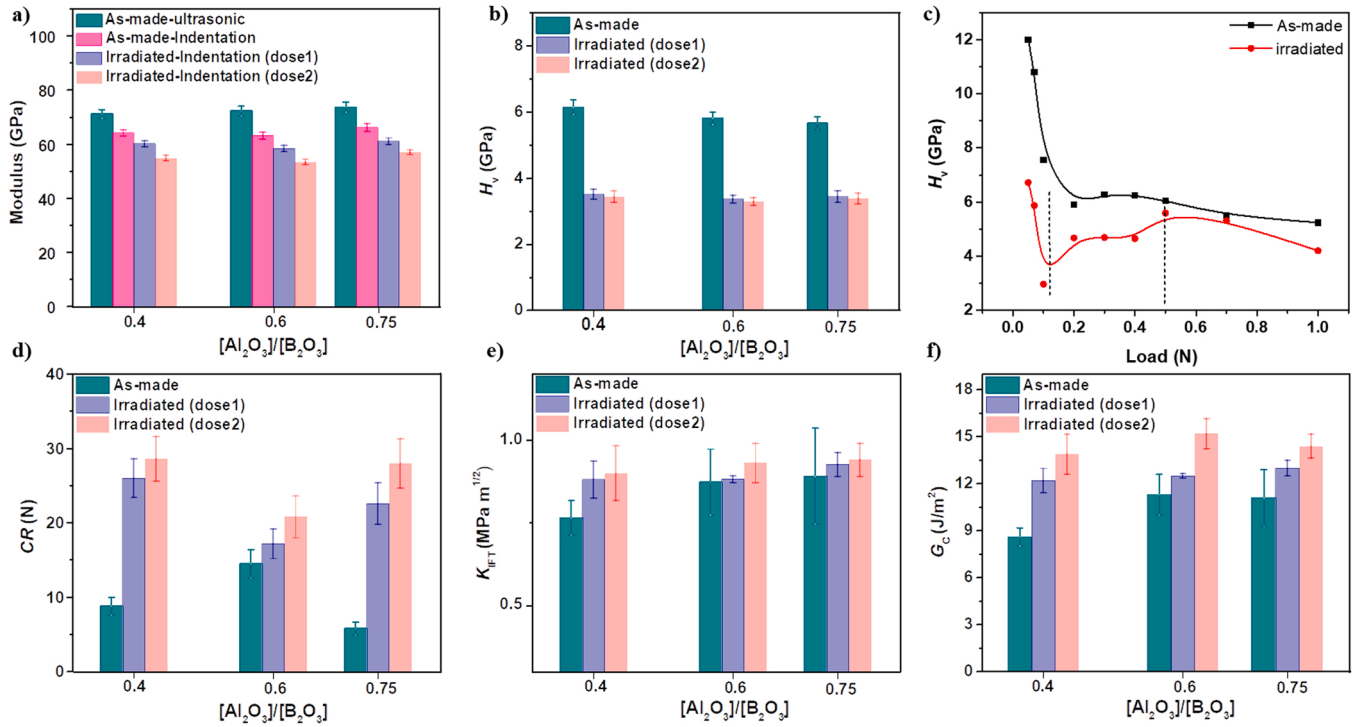

Fig. 6. (a) Young's modulus (E) of the as-made and irradiated CABS glasses as determined from ultrasonic echography or the load-depth indentation curve. Dose 1 and Dose 2 refer to irradiation does of $2.0{\cdot}10^{13}$ ions/cm^2 and $2.0{\cdot}10^{14}$ ions/cm^2, respectively. (b) Vickers hardness (H_V) of the irradiated glass and as-made glasses. (c) Load dependence of hardness for the CABS-0.4 glass. (d) Crack resistance (CR) from Vickers indentation of the as-made and irradiated CABS glasses. (e) Indentation fracture toughness (K_{IFT}) determined using a sharp 100° tip of the as-made and irradiated CABS glasses. (f) Calculated fracture energy (G_c) based on K_{IFT} data for the as-made and irradiated CABS glasses.

also experienced the most obvious $^{[4]}$B to $^{[3]}$B conversion after irradiation. Since fracture is closely related to the reorganization of atomic structure under deformation, which is challenging to characterize experimentally, we here use MD simulation to reveal the mechanism of irradiation-induced toughening in the following section.

3.4. Fracture simulations

To gain a deeper understanding of the structure-properties relationship of the irradiated CABS glasses, the fracture behavior of the as-made and irradiated glasses is simulated with MD. We simulated the mode I fracture of the glass samples with a precrack (see Section 2.3.4). As shown in Fig. 7a, the crack grows from the edges of the precrack and then propagates perpendicular to the loading direction upon tension. Comparing the fracture behaviors at a strain of 0.2, we clearly observe that while the as-made glass is almost fractured, the irradiated glass structures are still relatively intact with a more ductile fracture response. The fracture process of the two other compositions exhibit a similar behavior (see Fig. S18). Fig. 7b-d show the stress-strain curves of the three CABS glasses upon uniaxial fracture. The as-made glasses exhibit a fairly brittle response, which manifests itself by a sudden drop in the stress-strain curve after the crack starts to propagate. However, the irradiated samples feature an improved nanoductility by exhibiting a slower decay of stress after the crack initiation. This irradiation-induced nanoductility has also previously been observed in silica systems[56, 101]. Additionally, we also note that the slope of the stress-strain curves in the elastic region (strain $\varepsilon < 0.05$) decreases upon irradiation, indicating a reduced stiffness induced by irradiation. Interestingly, we find that the irradiated CABS-0.4 glasses exhibit a more ductile fracture without a lower yield stress, indicating a higher fracture energy after irradiation for this glass composition.

Based on the stress-strain curves, we determine the Young's modulus E and fracture energy G_c. As shown in Table 3, both the values and the trend of Young's modulus are in good agreement with the experimental values (see Fig. 6a). Although the fracture energies are slightly underestimated relative to the experimental values from indentation techniques (Fig. 6 f), the irradiation dependence on the fracture energy is fully captured by MD simulations. Specifically, the G_c values of all the CABS glasses increases after irradiation, with the CABS-0.4 sample increasing the most from the initially lowest G_c. We also note that the $^{[4]}$B to $^{[3]}$B conversion upon irradiation in the CABS-0.4 sample is the most pronounced, indicating that the $^{[4]}$B to $^{[3]}$B conversion is responsible for the irradiation induced nanoductility.

The origin of irradiation-induced nanoductility is further investigated by analyzing the bond switching activities of the network formers in the CABS glasses (i.e., Al, B, and Si atoms). Here, the fraction of bond switching atoms are categorized by comparing the CN of each atom with its initial CN at nonstrained state, i.e., whether atom will increase, decrease, or swap its neighbor atoms under tensile deformation. As shown in Fig. S19, all the bond switching activities increase with an increase in strain, indicating that the structural reorganization is closely related to bond switching to dissipate the strain energy[5]. Under deformation, most of the bond switching events are related to Al and B atoms. When the glass is subjected to irradiation, the fraction of swapped CN Al atoms increases significantly, while all the bond switching of B atoms also rise at varying degrees. Interestingly, although the CN of Al atoms do not exhibit large changes upon irradiation, the propensity for Al atoms to swap its CN significantly increase with increasing deposited energy. This can be attributed to the fact that the $^{[4]}$B to $^{[3]}$B conversion decreases the number of Ca atoms used for charge compensating $^{[4]}$B atoms, which in turn facilitates the increase in the number of non-bridging oxygens. As shown in Fig. S20, the Q_n units of Al atoms with less connectivity ($n < 4$, Q_n denotes Al atom connects with n bridging oxygens) increase upon irradiation, promoting the bond switching of Al atoms.

Meanwhile, the medium-range structure also changes upon

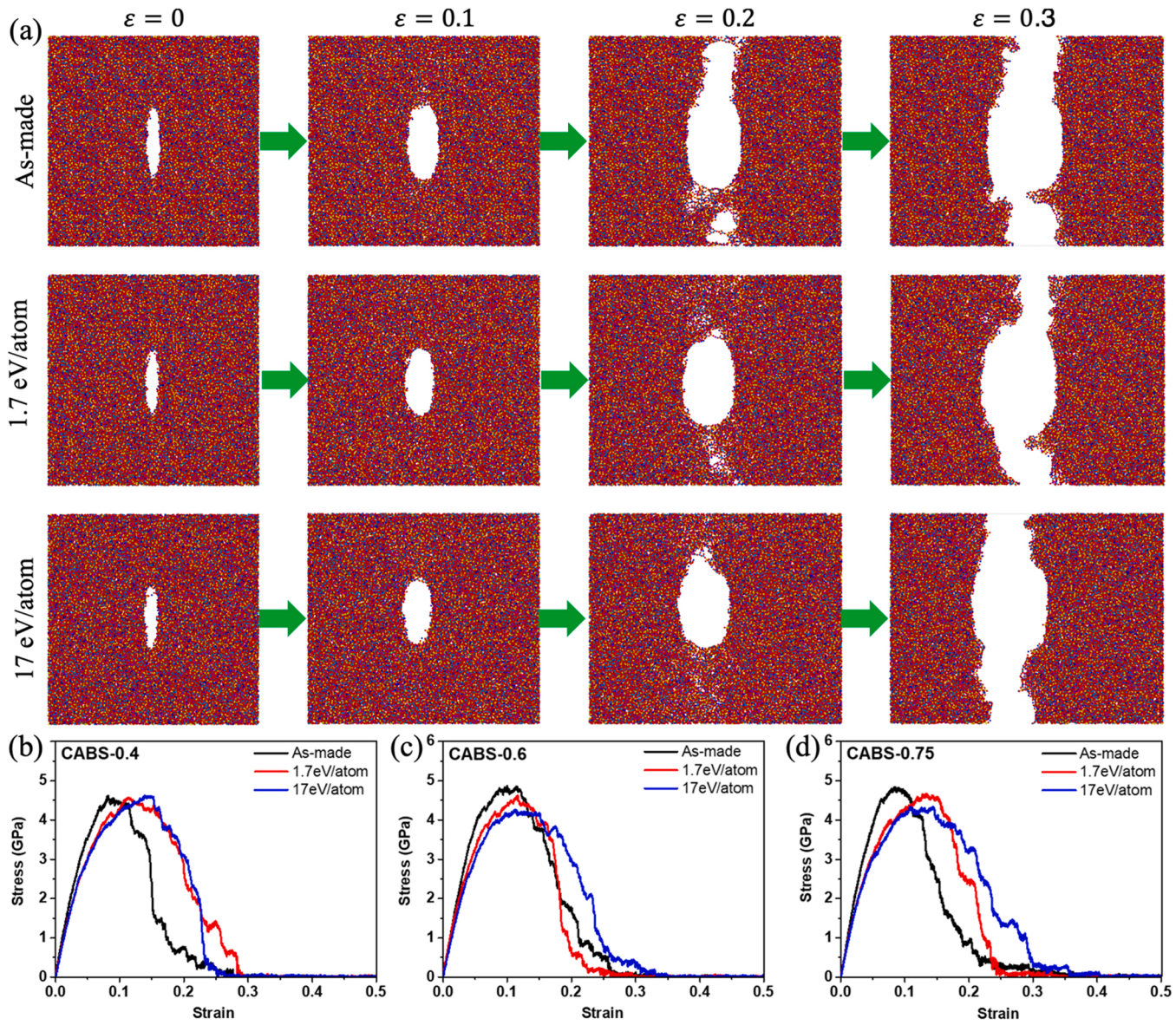

Fig. 7. (a) Evolution of fracture in the pre-cracked CABS-0.4 glass at tensile strains of 0, 0.1, 0.2, and 0.3. (b-d) Stress-strain curves of (b) CABS-0.4, (c) CABS-0.6, and (d) CABS-0.75 glasses subjected to different amounts of irradiation energies (0, 1.7, and 17 eV/atom).

Table 3
Young's modulus and fracture energy calculated based on MD simulations.

	Young's modulus E (GPa)			Fracture energy G_c (J/m^2)		
	As-made	1.7 eV/atom	17 eV/atom	As-made	1.7 eV/atom	17 eV/atom
CABS-0.4	71.2	60.4	61.4	4.1	4.4	5.9
CABS-0.6	78.3	63.5	60.6	4.9	4.7	5.0
CABS-0.75	78.8	61.5	60.9	4.3	4.7	5.0

irradiation to facilitate bond switching and leads to an improved nanoductility, e.g., the formation of small rings (less than four atoms), which are over-constrained and tend to reorganize upon deformation. This indicates that the irradiation-induced nanoductility can be attributed to the structural changes originating from the $^{[4]}$B to $^{[3]}$B conversion, which in turn promotes the propensity for bond switching of both Al and B atoms. In metallic glasses, the irradiation-induced ductility is found to be correlated with formation of liquid-like structures, which causes the deformation pattern to transition from localized shear banding to homogeneous shear flow[102,103]. The atoms with higher potential energy induced by irradiation are more likely to participate in shear transformations[104]. As such, the toughening mechanism induced by irradiation in oxide and metallic glasses can be both explained through the formation of atoms with high propensity for plastic rearrangement.

4. Conclusion

In this work, we have investigated the relation between structure and mechanical properties in CABS glasses subjected to irradiation through both experimental measurements and MD simulations. We find that the irradiation-induced structure changes in CABS glasses are mainly attributed to the boron speciation changes from $^{[4]}$B to $^{[3]}$B, which leads to a more open structure with an increased disorder at the medium-range length scale. The structure of CABS glasses with higher initial fraction of tetrahedral boron units are therefore found to be more susceptible to change upon irradiation. Upon irradiation of the glass surface

layers, the modulus and hardness decrease, while the crack resistance increases significantly. Specifically, crack resistance increased by more than 400% for the irradiated CABS-0.75 glass compared to the as-made one. In the case of hardness, the experiments performed at different loads showed that hardness first decreased with load, then increased slightly, and finally reached a constant value. This can be related to the decrease in the hardness of the μm-sized irradiated layer. Furthermore, both the experimental and simulation data show that the fracture energy also increases upon irradiation, with an improved nanoductility in the irradiated structures. This irradiation-induced nanoductility is attributed to the changes in medium-range structure, which facilitates bond switching of Al and B atoms. Interestingly, the CABS glass composition with the largest increase in *CR* and K_{IFT} is the one with the most $^{[4]}$B-rich structure, which is more susceptible to structural reorganization upon irradiation.

CRediT authorship contribution statement

Xiangting Ren: Methodology, Investigation, Writing – original draft. **Tao Du:** Formal analysis, Investigation, Writing – original draft. **Haibo Peng:** Investigation, Writing – review & editing. **Lars R. Jensen:** Investigation, Writing – review & editing. **Christophe A. N. Biscio:** Formal analysis, Writing – review & editing. **Lisbeth Fajstrup:** Formal analysis, Writing – Review & Editing. **Mathieu Bauchy:** Conceptualization, Writing – review & editing. **Morten M. Smedskjaer:** Conceptualization, Supervision, Writing – original draft.

Declaration of Competing Interest

The authors declare that they have no known competing financial interests or personal relationships that could have appeared to influence the work reported in this paper.

Data Availability

The raw and processed data required to reproduce these findings are available from the corresponding author upon request.

Acknowledgements

This work was supported by grants from the China Scholarship Council (No. 201906250152) to X.R., the Marie Skłodowska-Curie Individual Fellowship (No. 101018156) to T.D., the Independent Research Fund Denmark (No. 1026-00037B) to M.M.S., C.A.N.B. and L.F, the Fundamental Research Funds for the Central Universities of China (No. lzujbky-2021-kb11) to H.P., and the National Science Foundation (No. CMMI-1762292 and DMR-1944510) to M.B. We also thank Aalborg University for providing the computational resources through CLAAUDIA.

Appendix A. Supporting information

Supplementary data associated with this article can be found in the online version at doi:10.1016/j.mtcomm.2022.103649.

References

[1] L. Wondraczek, J.C. Mauro, J. Eckert, U. Kühn, J. Horbach, J. Deubener, T. Rouxel, Adv. Mater. 23 (2011) 4578–4586.
[2] J.C. Mauro, A. Tandia, K.D. Vargheese, Y.Z. Mauro, M.M. Smedskjaer, Chem. Mater. 28 (2016) 4267–4277.
[3] J. Luo, J. Wang, E. Bitzek, J.Y. Huang, H. Zheng, L. Tong, Q. Yang, J. Li, S.X. Mao, Nano Lett. 16 (2016) 105–113.
[4] K. Zheng, C. Wang, Y.-Q. Cheng, Y. Yue, X. Han, Z. Zhang, Z. Shan, S.X. Mao, M. Ye, Y. Yin, E. Ma, Nat. Commun. 1 (2010) 24.
[5] E.J. Frankberg, J. Kalikka, F.G. Ferré, L. Joly-Pottuz, T. Salminen, J. Hintikka, M. Hokka, S. Koneti, T. Douillard, M. Vanazzi, L. Roiban, J. Akola, F.D. Fonzo, E. Levänen, K. Masenelli-Varlot, Science (2019) 7.
[6] T. Du, H. Liu, L. Tang, S.S. Sørensen, M. Bauchy, M.M. Smedskjaer, ACS Nano 15 (2021) 17705–17716.
[7] G.D. Quinn, J.J. Swab, J. Eur. Ceram. Soc. 37 (2017) 4243–4257.
[8] T. To, Fracture Toughness and Fracture Surface Energy of Inorganic and Non-Metallic Glasses, These de doctorat, Rennes 1, 2019.
[9] M.B. Østergaard, S.R. Hansen, K. Januchta, T. To, S.J. Rzoska, M. Bockowski, M. Bauchy, M.M. Smedskjaer, Materials 12 (2019) 2439.
[10] J. Luo, J.C. Mauro, Transparent Silicate Glasses with High Fracture Toughness, WO2018017638A1, 2018.
[11] T. To, S.S. Sørensen, J.F.S. Christensen, R. Christensen, L.R. Jensen, M. Bockowski, M. Bauchy, M.M. Smedskjaer, ACS Appl. Mater. Interfaces 13 (2021) 17753–17765.
[12] T.M. Gross, J.J. Price, Front. Mater. 4 (2017).
[13] J.J. Price, G.S. Glaesemann, D.A. Clark, T.M. Gross, K.L. Barefoot, SID Symp. Dig. Tech. Pap., 40, 2009, pp. 1049–1051.
[14] T.M. Gross, J. Non-Cryst. Solids 358 (2012) 3445–3452.
[15] K.W. Peter, J. Non-Cryst. Solids 5 (1970) 103–115.
[16] A. Arora, D.B. Marshall, B.R. Lawn, M.V. Swain, J. Non-Cryst. Solids 31 (1979) 415–428.
[17] J.T. Hagan, J.Mater Sci 15 (1980) 1417–1424.
[18] J.D. Mackenzie, J. Am. Chem. Soc 46 (1963) 461–470.
[19] E.H. Yoffe, A. Philos. Mag, 46, 1982, pp. 617–628.
[20] T.M. Gross, J. Wu, D.E. Baker, J.J. Price, R. Yongsunthon, J. Non-Cryst. Solids 494 (2018) 13–20.
[21] S.G. Motke, S.P. Yawale, S.S. Yawale, Bull. Mater. Sci. 25 (2002) 75–78.
[22] X. Ren, P. Liu, S.J. Rzoska, B. Lucznik, M. Bockowski, M.M. Smedskjaer, Materials 14 (2021) 3450.
[23] G. Hj. Matzke, J.C. Della Mea, G. Dran, B. Linker, Tiveron, Nucl. Instrum. Methods Phys. Res. Sect. B Beam Interact. Mater. 46 (1990) 253–260.
[24] C.M. Jantzen, D.I. Kaplan, N.E. Bibler, D.K. Peeler, M. John Plodinec, J. Nucl. Mater. 378 (2008) 244–256.
[25] W. Yuan, H. Peng, M. Sun, X. Du, P. Lv, Y. Zhao, F. Liu, B. Zhang, X. Zhang, L. Chen, T. Wang, J. Chem. Phys. 147 (2017), 234502.
[26] M. Guan, X.Y. Zhang, K.J. Yang, T.T. Wang, F.F. Liu, M.L. Sun, X. Du, T.S. Wang, H.B. Peng, J. Non-Cryst. Solids 518 (2019) 118–122.
[27] D.A. Kilymis, J.M. Delaye, J. Non-Cryst. Solids 382 (2013) 87–94.
[28] D.A. Kilymis, J.-M. Delaye, J. Chem. Phys. 141 (2014), 014504.
[29] D.A. Kilymis, J. -M. Delaye, J. Non-Cryst. Solids 401 (2014) 147–153.
[30] D.A. Kilymis, J.-M. Delaye, S. Ispas, J. Chem. Phys. 145 (2016), 044505.
[31] M. Sebastiani, K.E. Johanns, E.G. Herbert, G.M. Pharr, Curr. Opin. Solid State Mater. Sci. 19 (2015) 324–333.
[32] G.M. Pharr, W.C. Oliver, F.R. Brotzen, J. Mater. Res. 7 (1992) 613–617.
[33] E. Broitman, Tribol. Lett. 65 (2016) 23.
[34] M. Wada, H. Furukawa, K. Fujita, Proc. 10th Int. Congr. Glass 11 (1974).
[35] K. Niihara, R. Morena, D.P.H. Hasselman, J. Mater. Sci. Lett. 1 (1982) 13–16.
[36] B.R. Lawn, M.V. Swain, J. Mater. Sci. 10 (1975) 113–122.
[37] A. Makishima, J.D. Mackenzie, J. Non-Cryst. Solids 12 (1973) 35–45.
[38] D.B. Marshall, R.F. Cook, N.P. Padture, M.L. Oyen, A. Pajares, J.E. Bradby, I. E. Reimanis, R. Tandon, T.F. Page, G.M. Pharr, B.R. Lawn, J. Am. Ceram. Soc. 98 (2015) 2671–2680.
[39] G.R. Anstis, P. Chantikul, B.R. Lawn, D.B. Marshall, J. Am. Ceram. Soc. 64 (1981) 533–538.
[40] G.R. Irwin, Fract. Hanbuck Phys. VI Elast. Plast., 1958, pp. 551–590.
[41] S. Plimpton, J. Comput. Phys. 117 (1995) 1–19.
[42] A. Stukowski, Model. Simul. Mater. Sci. Eng. 18 (2009), 015012.
[43] L. Deng, J. Du, J. Am. Ceram. Soc. 102 (2019) 2482–2505.
[44] J. Du Mol. Dyn. Simul. Disord. Mater. Netw. Glas. Phase-Change Mem. Alloys, Springer International Publishing C. Massobrio J. Du M. Bernasconi P.S. Salmon Cham 2015 157 180.
[45] F. Lodesani, M.C. Menziani, H. Hijiya, Y. Takato, S. Urata, A. Pedone, Sci. Rep. 10 (2020) 2906.
[46] P.H. Kuo, J. Du, J. Phys. Chem. C 123 (2019) 27385–27398.
[47] S.S. Sørensen, H. Johra, J.C. Mauro, M. Bauchy, M.M. Smedskjaer, Phys. Rev. Mater. 3 (2019), 075601.
[48] X. Lu, L. Deng, S. Gin, J. Du, J. Phys. Chem. B 123 (2019) 1412–1422.
[49] M. Wang, N.M. Anoop Krishnan, B. Wang, M.M. Smedskjaer, J.C. Mauro, M. Bauchy, J. Non-Cryst. Solids 498 (2018) 294–304.
[50] J.F. Ziegler, J.P. Biersack, in: D.A. Bromley (Ed.), Treatise Heavy-Ion Sci. Vol. 6 Astrophys. Chem. Condens. Matter, Springer US, Boston, MA, 1985, pp. 93–129.
[51] L. Martínez, R. Andrade, E.G. Birgin, J.M. Martínez, J. Comput. Chem. 30 (2009) 2157–2164.
[52] S. Nosé, Mol Phys 52 (1984) 255–268.
[53] N.M.A. Krishnan, B. Wang, Y. Yu, Y. Le Pape, G. Sant, M. Bauchy, Phys. Rev. X 7 (2017), 031019.
[54] N.M.A. Krishnan, B. Wang, G. Sant, J.C. Phillips, M. Bauchy, ACS Appl. Mater. Interfaces 9 (2017) 32377–32385.
[55] N.M.A. Krishnan, R. Ravinder, R. Kumar, Y. Le Pape, G. Sant, M. Bauchy, Acta Mater. 166 (2019) 611–617.
[56] R. Ravinder, A. Kumar, R. Kumar, P. Vangla, N.M.A. Krishnan, J. Am. Ceram. Soc. 103 (2020) 3962–3970.
[57] S. Le Roux, P. Jund, Comput. Mater. Sci. 49 (2010) 70–83.
[58] L. Guttman, J. Non-Cryst. Solids 116 (1990) 145–147.
[59] T.E. Faber, J.M. Ziman, Philos. Mag. J. Theor. Exp. Appl. Phys. 11 (1965) 153–173.
[60] Q. Zhou, Y. Shi, B. Deng, T. Du, L. Guo, M.M. Smedskjaer, M. Bauchy, J. Non-Cryst. Solids 573 (2021), 121138.

[61] Y. Onodera, S. Kohara, S. Tahara, A. Masuno, H. Inoue, M. Shiga, A. Hirata, K. Tsuchiya, Y. Hiraoka, I. Obayashi, K. Ohara, A. Mizuno, O. Sakata, J. Ceram. Soc. Jpn. 127 (2019) 853–863.
[62] Y. Hiraoka, T. Nakamura, A. Hirata, E.G. Escolar, K. Matsue, Y. Nishiura, Proc. Natl. Acad. Sci. 113 (2016) 7035–7040.
[63] Y. Onodera, S. Kohara, P.S. Salmon, A. Hirata, N. Nishiyama, S. Kitani, A. Zeidler, M. Shiga, A. Masuno, H. Inoue, S. Tahara, A. Polidori, H.E. Fischer, T. Mori, S. Kojima, H. Kawaji, A.I. Kolesnikov, M.B. Stone, M.G. Tucker, M.T. McDonnell, A.C. Hannon, Y. Hiraoka, I. Obayashi, T. Nakamura, J. Akola, Y. Fujii, K. Ohara, T. Taniguchi, O. Sakata, NPG Asia Mater. 12 (2020) 85.
[64] S. Hosokawa, J.-F. Bérar, N. Boudet, W.-C. Pilgrim, L. Pusztai, S. Hiroi, K. Maruyama, S. Kohara, H. Kato, H.E. Fischer, A. Zeidler, Phys. Rev. B 100 (2019), 054204.
[65] Y. Onodera, Y. Takimoto, H. Hijiya, T. Taniguchi, S. Urata, S. Inaba, S. Fujita, I. Obayashi, Y. Hiraoka, S. Kohara, N.P.G. Asia, NPG Asia Mater. 11 (2019) 1–11.
[66] Diode—Persistent Dmitriy, Homol. Softw. (2021).
[67] Dionysus2—Persistent Dmitriy, Homol. Softw. (2021).
[68] Y. Hiraoka, T. Nakamura, A. Hirata, E.G. Escolar, K. Matsue, Y. Nishiura, Proc. Natl. Acad. Sci. 113 (2016) 7035–7040.
[69] S.S. Sørensen, C.A.N. Biscio, M. Bauchy, L. Fajstrup, M.M. Smedskjaer, Sci Adv. 6 (2020), eabc2320.
[70] L. Brochard, G. Hantal, H. Laubie, F.J. Ulm, R.J.-M. Pellenq, (2013) 2471–2480.
[71] M. Bauchy, H. Laubie, M.J. Abdolhosseini Qomi, C.G. Hoover, F.-J. Ulm, R.J.-M. Pellenq, J. Non-Cryst. Solids 419 (2015) 58–64.
[72] B. Wang, Y. Yu, Y.J. Lee, M. Bauchy, Front. Mater. 2 (2015).
[73] T. Du, M. Blum, C. Chen, M.G. Muraleedharan, A.C.T. van Duin, P. Newell, Eng. Fract. Mech. 250 (2021), 107749.
[74] W.G. Hoover A. Phys. Rev 31 1985 1695 1697.
[75] A. Stukowski, JOM 66 (2014) 399–407.
[76] H. Li, Y. Su, L. Li, D.M. Strachan, J. Non-Cryst. Solids 292 (2001) 167–176.
[77] W.L. Konijnendijk, J.M. Stevels, J. Non-Cryst. Solids 20 (1976) 193–224.
[78] E.I. Kamitsos, G.D. Chryssikos, J. Mol. Struct. 247 (1991) 1–16.
[79] B.N. Meera, J. Ramakrishna, J. Non-Cryst. Solids 159 (1993) 1–21.
[80] K. Vignarooban, P. Boolchand, M. Micoulaut, M. Malki, W.J. Bresser, Europhys. Lett. 108 (2014) 56001.
[81] J. Krogh-Moe, J. Non-Cryst. Solids 1 (1969) 269–284.
[82] N. Ollier, T. Charpentier, B. Boizot, G. Wallez, D. Ghaleb, J. Non-Cryst. Solids 341 (2004) 26–34.
[83] T. Yano, N. Kunimine, S. Shibata, M. Yamane, J. Non-Cryst. Solids 321 (2003) 137–146.
[84] L.T. Chen, X.T. Ren, Y.N. Mao, J.J. Mao, X.Y. Zhang, T.T. Wang, M.L. Sun, T. S. Wang, M.M. Smedskjaer, H.B. Peng, J. Nucl. Mater. 552 (2021), 153025.
[85] K. Januchta, R.E. Youngman, A. Goel, M. Bauchy, S.L. Logunov, S.J. Rzoska, M. Bockowski, L.R. Jensen, M.M. Smedskjaer, Chem. Mater. 29 (2017) 5865–5876.
[86] R. Kumar, A. Jan, M. Bauchy, N.M.A. Krishnan, J. Am. Ceram. Soc. n/a (n.d.).
[87] J.-M. Delaye, S. Peuget, G. Bureau, G. Calas, J. Non-Cryst. Solids 357 (2011) 2763–2768.
[88] A. Jan, J.-M. Delaye, S. Gin, S. Kerisit, J. Non-Cryst. Solids 505 (2019) 188–201.
[89] S.M. Garner, Flexible Glass: Enabling Thin, Lightweight, and Flexible Electronics, John Wiley & Sons, 2017.
[90] K. Januchta, M. Bauchy, R.E. Youngman, S.J. Rzoska, M. Bockowski, M. M. Smedskjaer, Phys. Rev. Mater. 1 (2017), 063603.
[91] L. Chen, W. Yuan, S. Nan, X. Du, D.F. Zhang, P. Lv, H.B. Peng, T.S. Wang, Nucl. Instrum. Methods Phys. Res. Sect. B Beam Interact. Mater. 370 (2016) 42–48.
[92] L.-H. Kieu, J.-M. Delaye, C. Stolz, J. Non-Cryst. Solids 358 (2012) 3268–3279.
[93] H.B. Peng, M.L. Sun, K.J. Yang, H. Chen, D. Yang, W. Yuan, L. Chen, B.H. Duan, T. S. Wang, J. Non-Cryst. Solids 443 (2016) 143–147.
[94] S. Peuget, P.-Y. Noël, J.-L. Loubet, S. Pavan, P. Nivet, A. Chenet, Nucl. Instrum. Methods Phys. Res. Sect. B Beam Interact. Mater. 246 (2006) 379–386.
[95] J. de Bonfils, S. Peuget, G. Panczer, D. de Ligny, S. Henry, P.-Y. Noël, A. Chenet, B. Champagnon, J. Non-Cryst. Solids 356 (2010) 388–393.
[96] L.-H. Kieu, D. Kilymis, J.-M. Delaye, S. Peuget, Procedia Mater. Sci. 7 (2014) 262–271.
[97] B. Lawn. Fracture of Brittle Solids, second ed., Cambridge University Press, Cambridge, 1993.
[98] R.F. Cook, G.M. Pharr, J. Am. Ceram. Soc. 73 (1990) 787–817.
[99] S.S. Chiang, D.B. Marshall, A.G. Evans, J. Appl. Phys. 53 (1982) 298–311.
[100] H. Liu, B. Deng, S. Sundararaman, Y. Shi, L. Huang, J. Appl. Phys. 128 (2020), 035106.
[101] L. Tang, H. Liu, G. Ma, T. Du, N. Mousseau, W. Zhou, M. Bauchy, Mater. Horiz. 8 (2021) 1242–1252.
[102] D.J. Magagnosc, R. Ehrbar, G. Kumar, M.R. He, J. Schroers, D.S. Gianola, Sci. Rep. 3 (2013) 1096.
[103] Q. Xiao, L. Huang, Y. Shi, J. Appl. Phys. 113 (2013), 083514.
[104] D.Z. Chen, D. Jang, K.M. Guan, Q. An, W.A. Goddard, J.R. Greer, Nano Lett. 13 (2013) 4462–4468.